Diagrammatic Monte Carlo study of Fröhlich polaron dispersion in two and three dimensions

Thomas Hahn,[1] Sergei Klimin,[2] Jacques Tempere,[2] Jozef T. Devreese,[2] and Cesare Franchini[1]

[1]*University of Vienna, Faculty of Physics and Center for Computational Materials Science, Sensengasse 8, A-1090 Vienna, Austria*
[2]*Theory of Quantum and Complex Systems, Universiteit Antwerpen, Universiteitsplein 1, B-2610 Antwerpen, Belgium*

We present results for the solution of the large polaron Fröhlich Hamiltonian in 3 dimensions (3D) and 2 dimensions (2D) obtained via the diagrammatic Monte Carlo (DMC) method. Our implementation is based on the approach by Mishchenko [A. S. Mishchenko *et al.*, Phys. Rev. B **62**, 6317 (2000)]. Polaron ground state energies and effective polaron masses are successfully benchmarked with data obtained using Feynman's path integral formalism. By comparing 3D and 2D data, we verify the analytically exact scaling relations for energies and effective masses from 3D → 2D, which provides a stringent test for the quality of DMC predictions. The accuracy of our results is further proven by providing values for the exactly known coefficients in weak- and strong-coupling expansions. Moreover, we compute polaron dispersion curves which are validated with analytically known lower and upper limits in the small-coupling regime and verify the first-order expansion results for larger couplings, thus disproving previous critiques on the apparent incompatibility of DMC with analytical results and furnishing useful reference for a wide range of coupling strengths.

I. INTRODUCTION

Ever since the emergence of polaron theory in the 1930s [1], the concept of polarons has been applied to a wide variety of physical systems in which a particle is coupled to its environment, e.g., spin or magnetic polarons [2], exciton polarons [3], BEC-impurity polarons [4], and ripplonic polarons [5]. The polaron problem in its original form considers a single electron in a polar crystal interacting with the surrounding lattice. Due to Coulomb forces, the electron distorts the ions in its neighborhood, which creates a polarization that follows the electron as it moves through the crystal. This generated polarization acts back on the electron and so renormalizes electronic properties. The resulting quasiparticle consisting of the electron surrounded by the distorted lattice was termed a "polaron." Nowadays (cf. the review by Alexandrov and Devreese [6]) a more quantum mechanical picture of a polaron is used in which the electron dresses itself with a cloud of phonons.

Polarons may be classified according to the strength of the electron-phonon coupling (weak/strong) and the extension of the lattice distortion around the electron (small/large) [6,7]. Weak-coupling polarons dress themselves with only a small number of phonons $\bar{N} \ll 1$ leading to a slightly enhanced effective mass compared to the "bare" electron $(m_* - m) \ll m$. Strong-coupling polarons have more phonons in the cloud $\bar{N} \gg 1$ and a much larger effective mass $m_*/m \gg 1$. By $\bar{N}$ we denote the average number of phonons in the cloud, m_* is the effective mass of the polaron, and m the mass of the "bare" electron without coupling. Furthermore, a polaron is called a small polaron when the lattice distortion induced by the electron is of the same size as the lattice constant and a large polaron when the distortion extends over several lattice sites. Typically, the description of small polarons requires the treatment of short-range electron-phonon interaction and an explicit account of the lattice periodicity. Instead, the theory of large polarons assumes long-range forces and relies on the continuum approximation.

Studies of polarons are historically conducted in the framework of quantum field theory using effective quantum Hamiltonians [8,9]. More recently, first-principles methods based on density functional theory turned out to provide an accurate microscopic description of both large and small polarons [10,11]. The most famous model Hamiltonians go back to the 1950s to Fröhlich [8] and Holstein [9]. Both contain a term for a free particle H_e, a free phonon field H_{ph}, and for the particle-phonon interaction H_{e-ph}. While the Holstein Hamiltonian models small polarons, the Fröhlich Hamiltonian, which is the focus of the present study, describes large polarons and is given as

$$H = H_e + H_{ph} + H_{e-ph}, \tag{1}$$

$$H_e = \sum_{\mathbf{k}} \frac{k^2}{2} a_{\mathbf{k}}^\dagger a_{\mathbf{k}}, \tag{2}$$

$$H_{ph} = \sum_{\mathbf{q}} b_{\mathbf{q}}^\dagger b_{\mathbf{q}}, \tag{3}$$

$$H_{e-ph} = \sum_{\mathbf{k},\mathbf{q}} \left[V_d(\mathbf{q}) b_{\mathbf{q}}^\dagger a_{\mathbf{k}-\mathbf{q}}^\dagger a_{\mathbf{k}} + V_d^\dagger(\mathbf{q}) b_{\mathbf{q}} a_{\mathbf{k}+\mathbf{q}}^\dagger a_{\mathbf{q}} \right]. \tag{4}$$

Here $a_{\mathbf{k}}$ and $b_{\mathbf{q}}$ are destruction operators for a particle with wave vector $\mathbf{k}$ and a phonon with wave vector $\mathbf{q}$, respectively. $V_d(\mathbf{q})$ is the coupling function for a system in d dimensions and takes the form

$$V_3(\mathbf{q}) = i \left(\frac{2\sqrt{2}\pi\alpha}{A} \right)^{\frac{1}{2}} \frac{1}{q} \tag{5}$$

in 3 dimensions and

$$V_2(\mathbf{q}) = i\left(\frac{\sqrt{2}\pi\alpha}{A}\right)^{\frac{1}{2}}\frac{1}{\sqrt{q}} \tag{6}$$

in 2 dimensions [12]. In Eqs. (5) and (6), A is the d-dimensional volume of the system and α is the coupling constant which is material dependent and determines the strength of the electron-phonon interaction. Typical values for real materials are in the range $0 < \alpha < 5$ [13]. Units are chosen such that energy is measured in units of $\hbar\omega_0$ and length in units of $\sqrt{\hbar/m\omega_0}$ which leads to $\hbar = \omega_0 = m = 1$. In deriving and solving the Fröhlich Hamiltonian, it is a common practice to assume certain approximations: (i) the energy dispersion for the electron is parabolic with a band mass m, (ii) the phonon frequency $\omega(\mathbf{q}) = \omega_0$ is dispersionless and constant, (iii) the interaction is only between the electron and long-wavelength optical, longitudinal phonons, and (iv) the spatial extension of the polaron is larger than the lattice constant. In this paper, we exclusively focus on the Fröhlich model and we study the polaron dispersion law, i.e., the dependence of the ground state energy $E_0(k,\alpha)$ on the modulus of the total polaron momentum $k = |\mathbf{k}|$.

A large body of work [6] exists on solving the Fröhlich Hamiltonian, and most of it concerns the energy of the polaron at rest, $E_0(0,\alpha)$. Yet, so far no exact analytic solution was found. The most successful approach to calculate $E_0(0,\alpha)$ is Feynman's path integral formalism [14,15], a variational treatment that provides a very accurate upper bound for the polaron ground state energy for all coupling strengths as well as approximate values for the polaron effective mass. Early work on the behavior of the dispersion curve [16,17] allowed one to conclude that the energy-momentum relation starts off quadratically at low k (thus allowing one to define a polaron mass) but bends over when approaching the continuum edge $E_c(\alpha) = E_0(0,\alpha) + \hbar\omega_0$. Later it was found that in 3D the dispersion hits the continuum edge whereas for 2D it approaches it asymptotically, and upper and lower bounds for the dispersion were obtained [18–20]. These bounds, as well as some analytically known limits, constitute good benchmarks for any theory of the polaron dispersion.

More recently, the diagrammatic Monte Carlo method (DMC) was developed and applied to the 3-dimensional Fröhlich polaron [21,22]. It makes use of diagrammatic expansions of Green's functions and a Metropolis sampling algorithm to perform a random walk in the space of all Feynman diagrams. The DMC not only allows for the calculation of the ground state energies but as well the polaron dispersion curves, Z factors (quasiparticle weights), and phonon statistics. However, the DMC results [21,22] were criticized [19,20]: the reported results disagree with the analytically known second-order coefficient in α for the polaron ground state energy, as well as the large-α expansion coefficient.

The aim of the present paper is the application of our newly implemented DMC code to the solution of the Fröhlich Hamiltonian in both the 3-dimensional (3D) and the 2-dimensional (2D) case. To our knowledge, there do not exist any DMC results for the 2D Fröhlich polaron in the literature. We find that the present DMC results, both in 2D and 3D, agree with the analytically known limits, thus refuting the critique of the

DMC method formulated in [19,20]. In addition, we compare the obtained dispersion relations with analytic upper and lower bounds (where available) and a fitting function [20].

The structure of the paper is as follows. The DMC program is based on the seminal works of Prokof'ev [21] and Mishchenko [22], and is described in Sec. II. The numerical outcome is presented and discussed in Sec. III. We first benchmark our results for the 3D case with the reference data of Prokof'ev *et al.* [21] and Mishchenko *et al.* [22] as well as with results obtained from Feynman's path integral approach [15]. Furthermore, we show ground state energies $E_0(0,\alpha)$, polaron dispersions $E_0(k,\alpha)$, and effective masses $m_*(\alpha)$ for the 2D Fröhlich polaron and compare them to various scaling relations derived by Peeters and Devreese [23]. We also provide values for the exactly known weak- and strong-coupling coefficients. Finally, conclusive remarks are drawn in Sec. IV.

II. THEORY AND METHODOLOGY

In this section, we introduce the concepts of many-body Green's functions, diagrammatic expansions, and corresponding Feynman diagrams as well as the basic concepts of the diagrammatic Monte Carlo method. Necessary computational details of our code are also given in this section.

A. Green's functions and Feynman diagrams

To solve the Fröhlich Hamiltonian from Eq. (1) for the lowest energy eigenvalues, we make use of the Green's function formalism from many-body physics. In particular, we are interested in the one-electron-N-phonon Green's function in the momentum $(\mathbf{k}, \tilde{\mathbf{q}}_i)$–imaginary time (τ) representation at zero temperature, where we assume $\tau > 0$:

$$G^{(N)}(\mathbf{k}, \tau, \{\tilde{\mathbf{q}}_i\}) = \langle 0|b_{\tilde{\mathbf{q}}_N}(\tau)\ldots b_{\tilde{\mathbf{q}}_1}(\tau)a_{\mathbf{k}_1}(\tau)$$
$$\times a_{\mathbf{k}_1}^{\dagger}(0)b_{\tilde{\mathbf{q}}_1}^{\dagger}(0)\ldots b_{\tilde{\mathbf{q}}_N}^{\dagger}(0)|0\rangle. \tag{7}$$

The ket $|0\rangle$ in Eq. (7) is the electron and phonon vacuum state [24] and the operators are in the Heisenberg picture $a_{\mathbf{k}}(\tau) = e^{\tau H}a_{\mathbf{k}}e^{-\tau H}$. The total or polaron wave vector is given by $\mathbf{k} = \mathbf{k}_1 + \sum_i \tilde{\mathbf{q}}_i$ and is a conserved quantity [8].

By adding a complete set of polaron eigenstates $|\beta(\mathbf{k})\rangle$ to Eq. (7), with $H|\beta(\mathbf{k})\rangle = E_\beta(\mathbf{k})|\beta(\mathbf{k})\rangle$ and $H|0\rangle = E_v|0\rangle = 0$, the Green's function becomes

$$G^{(N)}(\mathbf{k}, \tau, \{\tilde{\mathbf{q}}_i\}) = \sum_\beta \left|\langle\beta(\mathbf{k})|a_{\mathbf{k}_1}^{\dagger}b_{\tilde{\mathbf{q}}_1}^{\dagger}\ldots b_{\tilde{\mathbf{q}}_N}^{\dagger}|0\rangle\right|^2 e^{-(E_\beta(\mathbf{k})-E_v)\tau}$$
$$= \sum_\beta Z_\beta^{(N)}(\mathbf{k}, \{\tilde{\mathbf{q}}_i\})e^{-E_\beta(\mathbf{k})\tau}. \tag{8}$$

The $Z_\beta^{(N)}$ factor measures the squared overlap between the polaron eigenstate $|\beta(\mathbf{k})\rangle$ and a state with one free electron and N free phonons. If $\tau \to \infty$, Eq. (8) shows that the term which contains the state with the lowest energy eigenvalue $E_0(\mathbf{k})$ is the dominant one in the sum. Therefore it is possible to retrieve $E_0(\mathbf{k})$ and the corresponding $Z_0^{(N)}(\mathbf{k}, \{\tilde{\mathbf{q}}_i\})$ factor for given $\mathbf{k}$ and $\{\tilde{\mathbf{q}}_i\}$ values from the asymptotic behavior of the Green's function at long imaginary times:

$$G^{(N)}(\mathbf{k}, \tau \to \infty, \{\tilde{\mathbf{q}}_i\}) = Z_0^{(N)}(\mathbf{k}, \{\tilde{\mathbf{q}}_i\})e^{-E_0(\mathbf{k})\tau}. \tag{9}$$
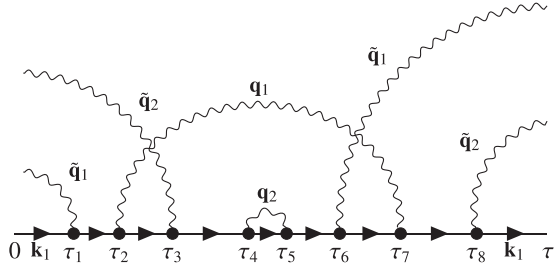
FIG. 1. Eighth-order diagram for $G^{(2)}(\mathbf{k},\tau,\tilde{\mathbf{q}}_1,\tilde{\mathbf{q}}_2)$. Note that diagrams in the expansion of $G^{(2)}$ have two phonon propagators attached to the diagram end. The total polaron wave vector $\mathbf{k} = \mathbf{k}_1 + \tilde{\mathbf{q}}_1 + \tilde{\mathbf{q}}_2$ is conserved at the vertices.

To calculate $G^{(N)}$, we expand the Green's function in a perturbation series [25]. Formally, this leads to an expression of the form

$$G^{(N)}(\mathbf{k},\tau,\{\tilde{\mathbf{q}}_i\}) = \sum_{n=0}^{\infty} \sum_{\xi_n} \int \cdots \int \mathcal{D}_{n,\xi_n}(\mathbf{k},\tau,\{\tilde{\mathbf{q}}_i\};\mathbf{x})d\mathbf{x},$$

(10)

where n labels the order of the perturbation expansion, ξ_n indexes different terms of the same order, and $\mathbf{x} = (\tau_1,\ldots,\tau_n,\mathbf{q}_1,\ldots,\mathbf{q}_k)$ is a vector of integration variables (times of interaction vertices and internal phonon wave vectors). Note the difference between external phonon wave vectors $\{\tilde{\mathbf{q}}_i\}$ appearing in the definition of $G^{(N)}$ and internal phonon wave vectors $\{\mathbf{q}_i\}$ over which is integrated. The integrands $\mathcal{D}_{n,\xi_n}$ are given as a product of free electron Green's functions $G_0(\mathbf{k},\tau_i - \tau_j)$, free phonon Green's functions $W_0(\mathbf{q},\tau_i - \tau_j)$, and squared interaction vertices $|V_d(\mathbf{q})|^2$. With the following simple rules it is possible to map all $\mathcal{D}_{n,\xi_n}$ functions to Feynman diagrams:

$$G_0(\mathbf{k}, \tau_i - \tau_j) = \underset{\tau_j \quad \mathbf{k} \quad \tau_i}{\longrightarrow} = e^{-k^2/2(\tau_i-\tau_j)}, \quad (11)$$

$$W_0(\mathbf{q}, \tau_i - \tau_j) = \underset{\tau_j \quad \mathbf{q} \quad \tau_i}{\sim\!\sim\!\sim} = e^{-\omega_0(\tau_i-\tau_j)}, \quad (12)$$

$$|V_d(\mathbf{q})|^2 = \underset{V_d(\mathbf{q}) \quad V_d^\dagger(\mathbf{q})}{\overset{\mathbf{q} \qquad \mathbf{q}}{\longrightarrow}} = \frac{(d-1)\sqrt{2}\pi\alpha}{Aq^{d-1}}. \quad (13)$$

This allows us to write the Green's function as an infinite series over Feynman diagrams. Odd orders in the perturbation series evaluate to zero because phonon operators appear linear in the interaction term of the Hamiltonian [Eq. (4)]. A typical diagram is presented in Fig. 1. It shows an eighth-order diagram of $G^{(2)}(\mathbf{k},\tau,\tilde{\mathbf{q}}_1,\tilde{\mathbf{q}}_2)$. All diagrams of $G^{(N)}$ have N external phonon propagators attached to the diagram end. The rules from Eqs. (11)–(13) can be used to translate a diagram back into its functional form. Integration has to be performed over all internal phonon wave vectors $\{\mathbf{q}_i\}$ and over all times $\{\tau_i\}$ so that their chronological order is maintained, e.g., $0 < \tau_1 < \tau_2 < \cdots < \tau_8 < \tau$ in Fig. 1. The total wave vector $\mathbf{k}$ is always conserved at interaction vertices. For example, the electron propagator between τ_1 and τ_2 in Fig. 1 must have the wave vector $\mathbf{k}_2 = \mathbf{k}_1 + \tilde{\mathbf{q}}_1$ so that $\mathbf{k} = \mathbf{k}_2 + \tilde{\mathbf{q}}_2$.

Input: initial diagram $\mathcal{D}^{(0)} \leftarrow (\{y^{(0)}\}; x_1^{(0)},\ldots,x_n^{(0)},n^{(0)},\xi_n^{(0)})$,
      update procedures $\{U_1,\ldots,U_k\}$,
      update probabilities $\{p(U_1),\ldots,p(U_k)\}$;
Output: histogram of $Q(\{y\})$;

initialize histogram[];
initialize diagram $\mathcal{D}_{cur} \leftarrow \mathcal{D}^{(0)}$;
while not converged **do**
    choose an update U_i from $\{U_1,\ldots,U_k\}$ with probability $p(U_i)$;
    propose a new diagram $\mathcal{D}_{new} \leftarrow (\{y'\}; x_1',\ldots,x_{n'}',n',\xi_{n'}')$ according to U_i;
    calculate acceptance ratio R;
    draw random uniform number r;
    if $R \geq r$ **then**
      accept the proposed diagram: $\mathcal{D}_{cur} \leftarrow \mathcal{D}_{new}$;
    else
      reject the proposed diagram: $\mathcal{D}_{cur} \leftarrow \mathcal{D}_{cur}$;
    end if
    histogram[$\{y\}$]$\leftarrow$ histogram[$\{y\}$]+1;
end while
return histogram;

FIG. 2. General workflow of the DMC algorithm. The algorithm returns the histogram of the function $Q(\{y\})$.

Expressing the Green's function in terms of Feynman diagrams does not solve the problem. It merely is a way to rewrite the expansion in a more accessible way. It is still necessary to sum the infinite series of integrals from Eq. (10).

B. Diagrammatic Monte Carlo

In Refs. [21,22,26] it was shown how to use the DMC method to numerically calculate a function $Q(\{y\})$ which is given in a diagrammatic expansion of the form

$$Q(\{y\}) = \sum_{n=0}^{\infty} \sum_{\xi_n} \int \cdots \int \mathcal{D}_{n,\xi_n}(\{y\};x_1,\ldots,x_n)dx_1\ldots dx_n.$$

(14)

The overall idea behind the DMC method is to interpret $Q(\{y\})$ as a distribution function for the external variables $\{y\}$ [21]. It then uses a Markov chain Monte Carlo (MCMC) procedure to simulate $Q(\{y\})$ by generating diagrams stochastically. This is achieved with a Metropolis-Hastings update scheme to accept or reject new diagrams in which the numerical values of $\mathcal{D}_{n,\xi_n}$ serve as statistical weights. The function $Q(\{y\})$ is obtained by collecting statistics for the external variables $\{y\}$, e.g., in the form of a histogram. At the heart of the DMC algorithm are updates that allow the Markov chain to explore the whole space of Feynman diagrams; i.e., the Markov chain has to be ergodic. It is therefore necessary to implement updates which change the order n, the topology ξ_n, external variables $\{y\}$, and internal variables x_i. Details on basic updating procedures and acceptance probabilities can be found in Refs. [21,22,26,27].

A general workflow of a DMC application is sketched in Fig. 2. Necessary requirements are a diagrammatic expansion of $Q(\{y\})$, updates $\{U_1,\ldots,U_k\}$, and probabilities $\{p(U_1),\ldots,p(U_k)\}$ with which the updates are chosen. The current diagram in each step is denoted by $\mathcal{D}_{\text{cur}}$ and

characterized by its parameter values $\mathbf{z} = (\{y\}; x_1, \ldots, x_n, n, \xi_n)$. The proposed diagram is called $\mathcal{D}_{\text{new}}$ with new parameters $\mathbf{z}' = (\{y'\}; x_1', \ldots, x_{n'}', n', \xi_{n'}')$. At the beginning, an initial diagram $\mathcal{D}^{(0)}$, e.g., a free electron propagator, is defined and the grid for the histogram is generated. During each Monte Carlo step an update U_i gets selected with probability $p(U_i)$. The update U_i proposes a new diagram $\mathcal{D}_{\text{new}}$ by changing one or more of the current parameters of $\mathbf{z}$ to $\mathbf{z}'$. Then a Metropolis-Hastings accept/reject step is performed with the following acceptance ratio (detailed balance is assumed):

$$R = \frac{p(U_i^\dagger) \mathcal{D}_{\text{new}} P(\mathbf{z}' \to \mathbf{z})}{p(U_i) \mathcal{D}_{\text{cur}} P(\mathbf{z} \to \mathbf{z}')}, \tag{15}$$

where $p(U_i^\dagger)$ is the probability of selecting the inverse update $U_i^\dagger$ of U_i and $P(\mathbf{z} \to \mathbf{z}')$ is an arbitrary probability density from which the new parameters $\mathbf{z}'$ are chosen. If $R \geqslant r$, where r is a uniform random number, $\mathcal{D}_{\text{new}}$ is accepted, otherwise rejected. Finally, the histogram at position $\{y\}$ is updated. These steps are repeated until convergence is achieved. Normalizing the resulting histogram leads to an estimation for $Q(\{y\})$.

C. DMC for the Fröhlich polaron

With the general procedure of the DMC algorithm at hand, it is fairly easy to apply it to the Fröhlich polaron. Comparing Eq. (10) with (14) leads to the following identifications:

  (i) $Q \leftrightarrow G^{(N)}$,

  (ii) $\{y\} \leftrightarrow \{\mathbf{k}, \tau, \{\tilde{\mathbf{q}}_i\}\}$,

  (iii) $\{x_1, \ldots, x_n\} \leftrightarrow \{\tau_1, \ldots, \tau_n, \mathbf{q}_1, \ldots, \mathbf{q}_k\}$.

The most straightforward way to obtain the lowest-energy eigenvalues $E_0(k, \alpha)$ of the Fröhlich Hamiltonian for a given $\mathbf{k}$ and α with the DMC method is to simulate $G^{(0)}(\mathbf{k}, \tau)$ and fit an exponential function to its long imaginary time behavior, as can be seen in Eq. (9). This was done in the original paper by Prokof'ev [21].

Mishchenko *et al.* [22] provided some improvements to this method. They simulated all $G^{(N)}(\mathbf{k}, \tau, \{\tilde{\mathbf{q}}_i\})$ up to some maximum value $N < N_{\text{max}}$ in a single run. It allowed them to introduce direct Monte Carlo estimators for the energy, effective mass, group velocity, and Z factors and to obtain results up to $\alpha = 20$.

In the present paper, we follow the approach by Mishchenko using estimators for the energy $e_{\text{est}}(\mathcal{D})$ and inverse effective polaron mass $m_{\text{est}}(\mathcal{D})$ making the curve-fitting procedure obsolete. A detailed exposition of the workflow can be found in Fig. 3. Values for the coupling constant α and the polaron wave vector $\mathbf{k}$ are defined as inputs before the simulation starts. The parameter μ is used as part of a guiding function of the form $e^{\mu\tau}$ to improve the sampling in τ space. In practice this means that each diagram is multiplied by $e^{\mu\tau}$ or simply by changing the value of the free electron Green's function to

$$G_0(\mathbf{k}, \tau_i - \tau_j, \mu) = e^{-(k^2/2 - \mu)(\tau_i - \tau_j)}. \tag{16}$$

For our calculations, we set μ slightly smaller than the true ground state energy, as recommended in Ref. [21]. We also have specified maximum values for the diagram length τ_{max}, the order n_{max}, and for the number of phonon propagators attached to the diagram end N_{max}. The value τ_{min} is used

---

Input: initial diagram $\mathcal{D}^{(0)} \leftarrow (\mathbf{k}, \tau^{(0)}, \{\tilde{\mathbf{q}}_i^{(0)}\}; \{\tau_i^{(0)}\}, \{\mathbf{q}_i^{(0)}\}, n^{(0)}, \xi_n^{(0)})$,
    update procedures $\{U_1, \ldots, U_k\}$,
    update probabilities $\{p(U_1), \ldots, p(U_k)\}$,
    values for: $\alpha, \mu, \mathbf{k}$,
    parameters: $\tau_{max}, \tau_{min}, n_{max}, N_{max}$;
Output: energy $E_0^{MC}(k, \alpha)$,
    inverse effective polaron mass $m_*^{MC}(\alpha)$;

initialize diagram $\mathcal{D}_{cur} \leftarrow \mathcal{D}^{(0)}$;
$E_0^{MC} \leftarrow 0, m_*^{MC} \leftarrow 0$;
$c \leftarrow 0$;
while not converged **do**
  choose an update U_i from $\{U_1, \ldots, U_k\}$ with probability $p(U_i)$;
  propose a new diagram $\mathcal{D}_{new} \leftarrow (\mathbf{k}, \tau', \{\tilde{\mathbf{q}}_i'\}; \{\tau_j'\}, \{\mathbf{q}_k'\}, n', \xi_{n'}')$ according to U_i;
  calculate acceptance ratio R;
  draw random uniform number r;
  if $R \geq r$ **then**
    accept the proposed diagram: $\mathcal{D}_{cur} \leftarrow \mathcal{D}_{new}$;
  else
    reject the proposed diagram: $\mathcal{D}_{cur} \leftarrow \mathcal{D}_{cur}$;
  end if
  if $\tau > \tau_{min}$ **then**
    $c \leftarrow c + 1$;
    $E_0^{MC} \leftarrow E_0^{MC} + e_{est}(\mathcal{D}_{cur})$;
    $m_*^{MC} \leftarrow m_*^{MC} + m_{est}(\mathcal{D}_{cur})$;
  end if
end while
return $E_0^{MC}/c, m_*^{MC}/c$;

FIG. 3. Detailed workflow of the DMC algorithm as it was used in this paper. The algorithm returns estimates for the lowest eigenenergy $E_0(k, \alpha)$ and the inverse of the effective polaron mass $1/m_*(\alpha)$ for given $\mathbf{k}$ and α values.

as a cutoff, in the sense that we only accumulate estimators if the current diagram length τ is greater than τ_{min}. In our case, $\tau_{\text{max}} = 50$ and $\tau_{\text{min}} = 5$. Values for n_{max} and N_{max} are dependent on the coupling strength α; τ_{max} and μ and should be chosen sufficiently higher than the average diagram order and average number of external phonons per diagram. The most important ingredients are the updates U_i. We implemented updates for adding and removing internal as well as external phonon propagators, changing the diagram length τ, stretching the diagram as a whole, shifting a single vertex in imaginary time, and swapping the phonon propagators of two adjacent vertices. All these updates and a derivation of the estimators are explained in detail in Ref. [22]. We only changed the arbitrary proposal probability distribution $P(\mathbf{z} \to \mathbf{z}')$ for some of the updates [see Eq. (15)]. Updates are addressed with the same probability $p(U_i) = p(U_j)$.

The basic concept is the same as in the general DMC algorithm, except that we accumulate estimators instead of a histogram (cf. Figs. 2 and 3). We start from an initial diagram $\mathcal{D}^{(0)}$. The accumulators for the energy E_0^{MC} and inverse effective mass m_*^{MC} as well as the counter c, for the number of diagrams with $\tau > \tau_{\text{min}}$, are set to zero. In the main loop, an update U_i is chosen with probability $p(U_i)$ and a new diagram $\mathcal{D}_{\text{new}}$ is proposed. It is accepted with probability $\min\{1, R\}$. After the accept/reject step, we check whether the
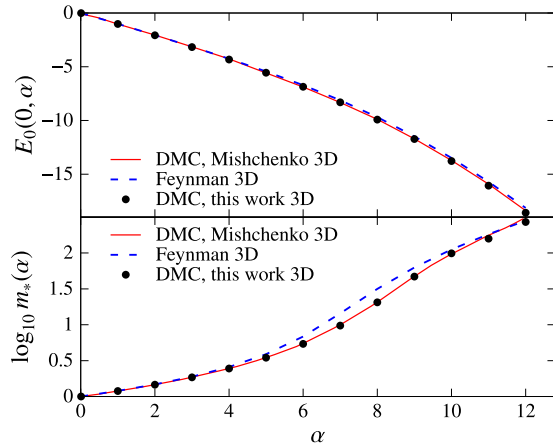
FIG. 4. Comparison of our results (circles) with previous DMC results by Mishchenko [22] (continuous lines) and with results obtained with Feynman's approach [15] (dashed lines). The top graph shows the polaron ground state energy $E_0(0,\alpha)$ and the bottom graph the logarithm of the polaron effective mass $\log m_*(\alpha)$ as a function of α.

current diagram length is greater than $\tau_{\min}$. If $\tau > \tau_{\min}$, c is increased by 1 and the energy and inverse effective mass estimator for the current diagram $\mathcal{D}_{\mathrm{cur}}$ are accumulated. The effective mass is calculated near $\mathbf{k} = 0$ using the quadratic approximation:

$$m_*(\alpha) = \left[\frac{\partial^2 E_0(k,\alpha)}{\partial k^2} \right]_{k=0}^{-1}. \qquad (17)$$

The loop is repeated until the energy and inverse effective mass estimates have converged. The final estimates are obtained by dividing the accumulators by c.

In Fig. 4, we reproduced some of the results from Ref. [22] to verify the correctness of our code. The top graph shows the polaron ground state energy and the bottom graph shows the logarithm of the effective mass as a function of α. Our data are in very good agreement with Mishchenko's data which lets us assume that our code gives reliable DMC results. The figure also displays results obtained with Feynman's variational treatment [15].

III. RESULTS AND DISCUSSION

In this section, we provide a more extensive discussion of the DMC results for the Fröhlich polaron in 3D and 2D. We show and discuss polaron ground state energies, effective polaron masses, and polaron dispersions for different coupling strengths and prove that DMC correctly accounts for the $3D \rightarrow 2D$ scaling relations. All energies are given in units of $\hbar\omega_0$ and lengths in units of $\sqrt{\hbar/m\omega_0}$.

A. Polaron ground state energy and effective mass

We first focus on our results for the polaron ground state energy $E_0(0,\alpha)$ (Fig. 5), i.e., the minimum of the polaron energy band, and for the effective polaron mass $m_*(\alpha)$ (Fig. 6) as a function of α for 3D and 2D systems. Both cases are compared to Feynman's approach [15] and with available
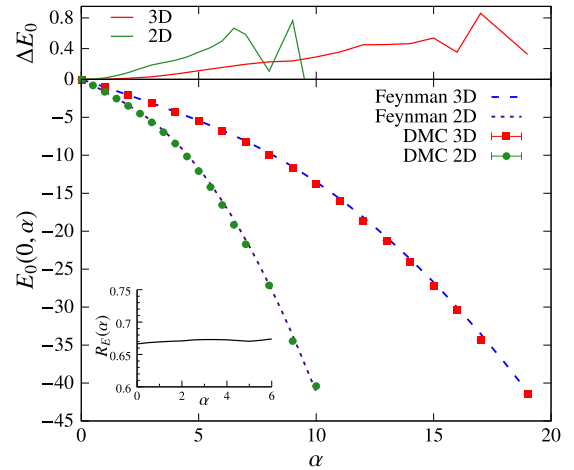
FIG. 5. Polaron energy $E_0(0,\alpha)$ as a function of the coupling constant α. The modulus of the total wave vector is $k = 0$. Results from the Feynman approach are shown as dashed lines. DMC results for 3D systems are depicted as squares and for 2D as circles. ΔE_0 is the difference between Feynman and DMC results. The inset shows the scaling ratio $R_E(\alpha) = E_0^{2D}(0,\alpha)/E_0^{3D}(0,3\pi\alpha/4)$ between our 2D and 3D DMC results.

DMC results in 3D [22] (Fig. 4). The corresponding numerical values are written in Table I (3D) and Table II (2D).

Feynman results in 2D have been obtained from the 3D results via scaling relations [23,28,29]. These scaling relations are exact for the Feynman polaron energy and Feynman polaron mass:

$$E_0^{2D}(0,\alpha) = \frac{2}{3} E_0^{3D}(0,3\pi\alpha/4), \qquad (18)$$

$$\frac{m_*^{2D}(\alpha)}{m^{2D}} = \frac{m_*^{3D}(3\pi\alpha/4)}{m^{3D}}. \qquad (19)$$

For $\alpha = 0$ the polaron does not form and therefore $E_0 = 0$ and $m_*(0) = m$. As expected, with increasing electron-phonon
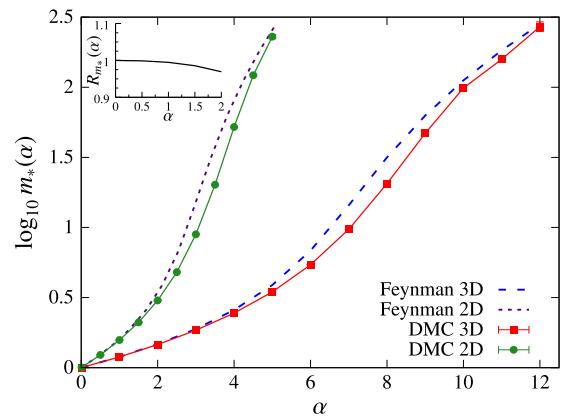
FIG. 6. Logarithm of the polaron effective mass $m_*(\alpha)$ as a function of the coupling constant α. Results from the Feynman approach are shown as dashed lines. DMC results for 3D systems are depicted as squares and for 2D as circles. The inset shows the scaling ratio $R_{m_*}(\alpha) = m_*^{2D}(\alpha)/m_*^{3D}(3\pi\alpha/4)$ between our 2D and 3D DMC results.

TABLE I. Ground state energies $E_0(0,\alpha)$ and effective masses $m_*(\alpha)$ in 3D from the DMC and Feynman method [15]. Values in parentheses stand for the uncertainty in the DMC simulation; e.g., $-1.01662(47)$ has a sample standard error of 4.7×10^{-4}.

α	E_0 DMC	E_0 Feynman	m_* DMC	m_* Feynman
1	$-1.01662(47)$	-1.0130308	$1.19396(2)$	1.1955147
2	$-2.06957(84)$	-2.0553559	$1.46166(7)$	1.4718919
3	$-3.16829(136)$	-3.1333335	$1.85047(13)$	1.8889540
4	$-4.32490(211)$	-4.2564809	$2.45196(57)$	2.5793104
5	$-5.55297(296)$	-5.4401445	$3.47194(180)$	3.8856197
6	$-6.86647(287)$	-6.7108710	$5.41952(625)$	6.8383564
7	$-8.31039(309)$	-8.1126875	$9.7130(268)$	14.394070
8	$-9.92206(606)$	-9.6953709	$20.55(14)$	31.569255
9	$-11.72535(701)$	-11.485786	$46.90(78)$	62.751527
10	$-13.7820(136)$	-13.490437	$98.8(3.3)$	111.81603
11	$-16.0660(127)$	-15.709808	$158.2(4.6)$	183.12497
12	$-18.5943(240)$	-18.143395	$270.1(20.0)$	281.62189
13	$-21.2434(249)$	-20.790681		412.78190
14	$-24.1151(369)$	-23.651278		582.58390
15	$-27.2629(359)$	-26.724904		797.49838

coupling the polaron energy $E_0(0,\alpha)$ decreases and the effective mass increases as a consequence of the progressive localization of the polaron band. This effect is stronger in 2D than in 3D and explains the steeper curves in 2D.

Overall, our DMC data agree very well with the Feynman results in the entire range of coupling strength, in particular for what concerns the polaron energy (Fig. 5). The only sizable deviation is observed for the effective mass in the intermediate-coupling regime, for which Feynman's approach gives considerably higher values than the DMC (Fig. 6). Both the DMC results and the variational results obey the scaling laws (18) and (19). This can be seen in the insets of Figs. 5 and 6 where we show the ratios $R_E(\alpha) = E_0^{2D}(0,\alpha)/E_0^{3D}(0,3\pi\alpha/4)$ and $R_{m_*}(\alpha) = m_*^{2D}(\alpha)/m_*^{3D}(3\pi\alpha/4)$ between our DMC results in 2D and 3D. However, the uncertainty in the Monte Carlo calculations of m_*^{2D} for $\alpha > 2$ worsens the stability of the scaling relation of the effective mass at large α. The reason for this low performance is that the effective mass estimator actually calculates the inverse of the effective mass rather than the effective mass itself [22]. Since the polaron mass grows very fast with increasing coupling, its inverse becomes very small, which unavoidably worsens the accuracy of theresults.

To test the accuracy of our calculations, we have also retrieved values for the exactly known weak-coupling coefficients q_1 and q_2

$$E_0(0,\alpha) = -q_1\alpha - q_2\alpha^2 + O(\alpha^3) \tag{20}$$

TABLE II. Ground state energies $E_0(0,\alpha)$ and effective masses $m_*(\alpha)$ in 2D from the DMC and Feynman method [15]. Values in parentheses stand for the uncertainty in the DMC simulation; e.g., $-1.64348(23)$ has a sample standard error of 2.3×10^{-4}.

α	E_0 DQMC	E_0 Feynman	m_* DQMC	m_* Feynman
1	$-1.64348(23)$	-1.62321	$1.57437(8)$	1.59966
2	$-3.48333(62)$	-3.39482	$3.01609(21)$	3.40982
3	$-5.66337(46)$	-5.47667	$8.94191(730)$	15.2085
4	$-8.45543(149)$	-8.20738	$52.108(341)$	81.1684
5	$-12.08288(610)$	-11.7281	$229.3(7.8)$	257.452
6	$-16.5403(269)$	-16.0402	$601.9(46.0)$	609.244
7	$-21.7231(566)$	-21.1408		
8	$-27.1346(802)$	-27.0283		
9	$-34.4669(370)$	-33.7021		
10	$-40.4139(379)$	-41.1602		

and the strong-coupling coefficient γ

$$\lim_{\alpha\to\infty} E_0(0,\alpha)/\alpha^2 = -\gamma. \tag{21}$$

The exact [19,28] and DMC values for these coefficients, listed in Table III, are in very good agreement. However, a word of caution is needed here: the coefficients are obtained with a simple curve-fitting procedure and the final numerical values are highly sensitive to the range of α values included in the fitting process. We have computed q_1 and q_2 using $\alpha < 0.85$ and $\alpha < 0.2$, in 3D and 2D respectively, whereas for γ we have included values in the range $9 \leqslant \alpha < 18$ (3D) and $4 \leqslant \alpha < 9$ (2D).

Gerlach, Kalina, and Smondyrev [19] correctly point out that the (3D) second-order perturbative result $q_2 = 0.0126$ obtained by Mishchenko using DMC [22] deviates from Röseler's [30] exact result $q_2 = 0.01592\ldots$, but we surmise that they incorrectly concluded that the DMC results $E_0(0,\alpha)$ are incompatible with Röseler's results. Here, we resolve this issue by providing the calculated DMC values explicitly, showing that there is no discrepancy. Both for the 3D and the 2D case, it can be seen in Table III that the DMC technique yields accurate estimates for q_2, as well as for the other analytically known expansion coefficients q_1 and γ.

B. Polaron dispersion

In Fig. 7, we display some dispersion curves in 3D and 2D for selected values of α. The results have been shifted so that the ground state energy at $k = 0$ is $E_0(0,\alpha) = 0$. This makes a comparison between different α values easier. As expected, $E_0(k,\alpha)$ increases monotonically as a function of k and becomes more flat with increasing coupling. This reflects the tendency to form more localized bands as the

TABLE III. Exactly known (exact) vs calculated (calc.) expansion coefficients of $E_0(0,\alpha)$ for the weak- and strong-coupling limit. The coefficients were obtained using different ranges of α in 2D and 3D. In 2D, we have included $\alpha < 0.2$ for computing q_1 and q_2 and $4 \leqslant \alpha < 9$ for γ. The corresponding 3D ranges are $\alpha < 0.85$ (q_1 and q_2) and $9 \leqslant \alpha < 18$ (γ).

	q_1 exact	q_1 calc.	q_2 exact	q_2 calc.	γ exact	γ calc.
3D	1.0	$0.9999 \pm 3.8 \times 10^{-4}$	0.01592	$0.01588 \pm 9.1 \times 10^{-4}$	0.1085	$0.10805 \pm 7.7 \times 10^{-4}$
2D	1.5708	$1.57084 \pm 1.7 \times 10^{-4}$	0.06397	$0.06483 \pm 2.8 \times 10^{-3}$	0.4047	$0.40236 \pm 3.8 \times 10^{-3}$

FIG. 7. Polaron energy $E_0(k,\alpha) - E_0(0,\alpha)$ as a function of the modulus of the total wave vector k in 3D (left, for coupling constants $\alpha = 1.0, 2.0$, and 3.0) and 2D (right, $\alpha = 0.5, 1.0$, and 1.5). The continuum edge is shown at $E_c(k) = 1$.

electron-phonon coupling strength becomes stronger, an effect that is more intense in the more localized 2D limit, where the dispersion curves bend over more sharply. Clearly, this behavior correlates with the polaron effective mass since it is defined as the inverse of the curvature of the energy band at $k = 0$ (see Fig. 6).

For large k, the energy curve approaches the so called "continuum edge" $E_c(\alpha)$ defined as the energy value:

$$E_c(\alpha) = E_0(0,\alpha) + \hbar\omega_0 = E_0(0,\alpha) + 1, \qquad (22)$$

i.e. the energy value which is one phonon excitation quantum or unity (in our units) above the ground state energy. An important difference between the 3D and 2D case is that in 3D the dispersion curve crosses the continuum edge at a finite critical wave vector length $k_c(\alpha)$. Instead, in 2D, it has been proven that this edge constitutes an asymptote and is approximated from below as $k \to \infty$ [18–20].

For small α, there exist rigorous upper and lower bounds for the polaron dispersion [20] that restrict this dispersion to a narrow domain. In the top row of Fig. 8, the DMC results are shown together with these bounds for $\alpha = 0.068$, the value of the coupling strength for GaAs. Our results lie in between the bounds, close to the upper bound, both in 3D (upper left panel of Fig. 8) and 2D (upper right panel). The strict lower bound only exists for small values of the coupling strength: $\alpha = 0.5$ already lies outside the range where this lower bound can be found.

Gerlach and Smondyrev [20] propose a fitting function for the dispersion. This fit is based on a rescaling of the upper bound formula, to obtain the correct gap between bottom of the band and the continuum edge, while maintaining the effective mass. As shown in the lower left panel of Fig. 8, the DMC results for the 3D case for $\alpha = 0.5$ lie below both the variational upper bound and the Gerlach-Smondyrev dispersion. The same conclusion can be drawn for the 2D case, shown in the lower right panel of Fig. 8.

We now focus on the 3D case, in which the dispersion reaches the continuum edge at a given k_c. Up to lowest order in α,

$$k_c(\alpha) = \sqrt{2} + \left(\frac{\pi}{2} - 1\right)\frac{\alpha}{\sqrt{2}} + O(\alpha^2). \qquad (23)$$

In Table IV, we compare for several α values the critical wave number obtained (i) with DMC, (ii) with the first-order approximation, Eq. (23), and (iii) using the Gerlach-Smondyrev dispersion. At small coupling strength $\alpha = 0.068$, all three approaches yield the same result. However, as α is increased slightly (remaining in the regime where the lowest-order approximation can be expected to be valid), the result obtained from the Gerlach-Smondyrev dispersion drops below the value found by the other two approaches. The value of k_c in the Gerlach-Smondyrev approach is 3% resp. 8% smaller than the DMC result for $\alpha = 0.5$ and 1.

Previously [20], this discrepancy was blamed on the fact that the DMC method supposedly failed to reproduce even the known q_2 parameter (the coefficient of α^2), whereas the fitting function is claimed to be good up to order α^3. However, as we have shown in the previous subsection, this explanation cannot hold since contrary to what was believed earlier, the DMC does reproduce the q_2 value with high accuracy. The Gerlach-Smondyrev dispersion is not the result of variational minimization, nor is it a rigorous lower bound: rather it is an *ad hoc* proposal that rescales the best variational upper bound to give the correct known limits. Keeping in mind that the DMC calculation takes many phonons into account (i.e., goes well beyond order α in the diagrams), we can conclude that the DMC results indicate that this fitting procedure is not appropriate for $\alpha \geqslant 0.5$.

IV. SUMMARY AND CONCLUSION

The diagrammatic Monte Carlo is a powerful method which has proven to work in many applications for many different systems [31–36]. For this paper, we have implemented a DMC

TABLE IV. Critical wave vectors $k_c(\alpha)$ for coupling constants $\alpha = 0.068$, $\alpha = 0.5$, and $\alpha = 1.0$. Listed are results from our DMC calculations, from Eq. (23), which is valid up to first order in α, as well as from the fitting function from Ref. [20].

	$\alpha = 0.068$	$\alpha = 0.5$	$\alpha = 1.0$
DMC, this work	1.440	1.615	1.833
Result to order α, Eq. (23)	1.442	1.616	1.818
Gerlach and Smondyrev, Ref. [20]	1.442	1.570	1.697
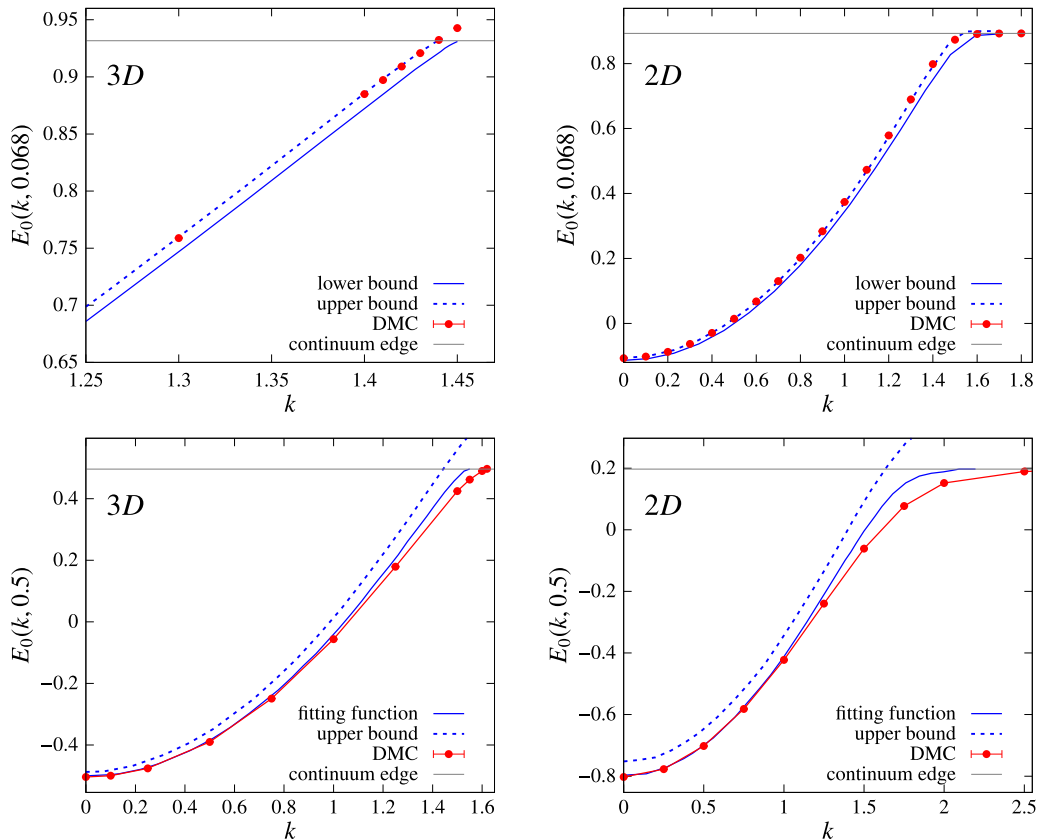
FIG. 8. Polaron energy $E_0(k,\alpha)$ in 3D (left) and 2D (right) as a function of the modulus of the total wave vector k for coupling constant $\alpha = 0.068$ (top row) and $\alpha = 0.5$ (bottom row). Lower and upper bounds and a fitting function to the dispersion are taken from Ref. [20].

code based on the Refs. [21,22] and applied it to the solution of the large polaron Fröhlich Hamiltonian in 3D and 2D. We benchmarked our code with existing DMC results for the 3D case to verify its correctness and then computed polaron ground state energies, effective polaron masses, and polaron dispersion curves in 2D and 3D.

In summary, our data confirm that the effect of electron-phonon coupling is enhanced in 2D compared to 3D, and this is reflected in all computed physical quantities. Concerning the ground state energies, the DMC results are in very good agreement with those obtained by Feynman's approach [15] and we have demonstrated that they obey the scaling relations between 3D and 2D [23]. The reliability of the DMC procedure is further corroborated by the calculations of the coefficients used for the weak- and strong-coupling regime, which are almost identical to the exactly known values. This refutes a claim [19] that the DMC technique is not able to correctly obtain the q_2 coefficients. Regarding the effective polaron mass, the DMC performance becomes slightly less satisfactory at stronger coupling. This inaccuracy should be traced back to the numerical errors involved in the calculation of the inverse of the effective mass. Alternative definitions of the polaron effective mass have been proposed in the literature, which could be possibly tested in future work to assess and compare the performance of DMC and path integral approaches [37,38].

One of the most interesting outcomes of the present study is the polaron dispersion curves. The DMC calculations reproduce very well the different behavior seen in 2D and 3D: in 2D the energy curve approaches the continuum edge asymptotically from below, whereas in 3D it reaches the continuum edge at a finite critical k_c. For small α (=0.068, a realistic value for a material like GaAs), the DMC dispersion as well as the k_c are in very good agreement with the known lower and upper limits derived from the variational approach of Gerlach and Smondyrev [20]. For larger α ($\alpha = 0.5$, 1.0), the DMC data agree well with the first-order expansion results, but deviate from the values based on a proposed fitting function for the dispersion. While the DMC technique cannot validate the fitting procedure proposed by Gerlach and Smondyrev for $\alpha \geqslant 0.5$, it does suggest that up to $\alpha \approx 1$ the first-order expansion result of Eq. (23) already provides an accurate estimate of k_c.

ACKNOWLEDGMENTS

[1] L. Landau, Phys. Z. Sowjetunion **3**, 664 (1933).

[2] E. L. Nagaev, Phys. Status Solidi B **65**, 11 (1974).

[3] H. Haken, in *Polarons and Excitons*, edited by C. Kuper and G. Whitfield (Plenum, New York, 1963), pp. 295–322.

[4] A. Miller, D. Pines, and P. Nozières, Phys. Rev. **127**, 1452 (1962).

[5] S. A. Jackson and P. M. Platzman, Phys. Rev. B **24**, 499 (1981).

[6] A. S. Alexandrov and J. T. Devreese, *Advances in Polaron Physics*, Springer Series in Solid-State Sciences (Springer-Verlag, Berlin, 2010).

[7] E. Rashba, in *Encyclopedia of Condensed Matter Physics*, edited by F. Bassani, G. L. Liedl, and P. Wyder (Elsevier, Oxford, 2005), pp. 347–355.

[8] H. Fröhlich, Adv. Phys. **3**, 325 (1954).

[9] T. Holstein, Ann. Phys. (NY) **8**, 325 (1959).

[10] M. Setvin, C. Franchini, X. Hao, M. Schmid, A. Janotti, M. Kaltak, C. G. Van de Walle, G. Kresse, and U. Diebold, Phys. Rev. Lett. **113**, 086402 (2014).

[11] K. Miyata, D. Meggiolaro, M. T. Trinh, P. P. Joshi, E. Mosconi, S. C. Jones, F. De Angelis, and X.-Y. Zhu, Sci. Adv. **3**, e1701217 (2017).

[12] F. M. Peeters, W. Xiaoguang, and J. T. Devreese, Phys. Rev. B **33**, 3926 (1986).

[13] J. T. Devreese, Phys. Scr. **1989**, 309 (1989).

[14] R. P. Feynman, Phys. Rev. **97**, 660 (1955).

[15] R. Rosenfelder and A. W. Schreiber, Phys. Lett. A **284**, 63 (2001).

[16] G. Whitfield and R. D. Puff, Phys. Rev. **139**, A338 (1965).

[17] J. Appel, in *Solid State Physics (Advances in Research and Applications)*, edited by F. Seitz, D. Turnbull, and H. Ehrenreich (Academic Press, New York, 1968), Vol. 21, pp. 193–391.

[18] B. Gerlach and F. Kalina, Phys. Rev. B **60**, 10886 (1999).

[19] B. Gerlach, F. Kalina, and M. Smondyrev, Phys. Status Solidi B **237**, 204 (2003).

[20] B. Gerlach and M. A. Smondyrev, Phys. Rev. B **77**, 174303 (2008).

[21] N. V. Prokof'ev and B. V. Svistunov, Phys. Rev. Lett. **81**, 2514 (1998).

[22] A. S. Mishchenko, N. V. Prokof'ev, A. Sakamoto, and B. V. Svistunov, Phys. Rev. B **62**, 6317 (2000).

[23] F. M. Peeters and J. T. Devreese, Phys. Rev. B **36**, 4442 (1987).

[24] D. Pines, in *Polarons and Excitons*, edited by C. Kuper and G. Whitfield (Plenum, New York, 1963), pp. 155–170.

[25] G. Mahan, *Many-Particle Physics*, Physics of Solids and Liquids (Springer US, 2000).

[26] A. S. Mishchenko, Phys. Usp. **48**, 887 (2005).

[27] K. V. Houcke, E. Kozik, N. Prokof'ev, and B. Svistunov, Phys. Proc. **6**, 95 (2010).

[28] W. Xiaoguang, F. M. Peeters, and J. T. Devreese, Phys. Rev. B **31**, 3420 (1985).

[29] F. M. Peeters, X. Wu, and J. T. Devreese, Phys. Rev. B **37**, 933 (1988).

[30] J. Röseler, Phys. Status Solidi **25**, 311 (1968).

[31] J. Vlietinck, J. Ryckebusch, and K. Van Houcke, Phys. Rev. B **87**, 115133 (2013).

[32] E. A. Burovski, A. S. Mishchenko, N. V. Prokof'ev, and B. V. Svistunov, Phys. Rev. Lett. **87**, 186402 (2001).

[33] A. S. Mishchenko, N. Nagaosa, and N. Prokof'ev, Phys. Rev. Lett. **113**, 166402 (2014).

[34] A. S. Mishchenko, N. Nagaosa, N. V. Prokof'ev, A. Sakamoto, and B. V. Svistunov, Phys. Rev. Lett. **91**, 236401 (2003).

[35] J. Vlietinck, J. Ryckebusch, and K. Van Houcke, Phys. Rev. B **89**, 085119 (2014).

[36] J. Vlietinck, W. Casteels, K. V. Houcke, J. Tempere, J. Ryckebusch, and J. T. Devreese, New J. Phys. **17**, 033023 (2015).

[37] D. C. Khandekar, K. V. Bhagwat, and S. V. Lawande, Phys. Rev. B **37**, 3085 (1988).

[38] V. Sa-yakanit and K. Tayanasanti, Phys. Rev. B **57**, 8739 (1998).